Title

Short-Range Order and Unusual Modes of Nickel Redox in a Fluorine-Substituted Disordered Rocksalt Oxide Lithium-Ion Cathode

Journal

Chemistry of Materials, 30(19)

ISSN

0897-4756

Authors

Clément, RJ
Kitchaev, D
Lee, J
et al.

Publication Date

2018-10-09

DOI

10.1021/acs.chemmater.8b03794

Peer reviewed

Short-Range Order and Unusual Modes of Nickel Redox in a Fluorine-Substituted Disordered Rocksalt Oxide Lithium-Ion Cathode

Raphaële J. Clément,[a]* Daniil Kitchaev,[b] Jinhyuk Lee,[a†] Gerbrand Ceder[a,c]

[a]Department of Materials Science and Engineering, University of California, Berkeley, CA 94720, USA.

[b]Department of Materials Science and Engineering, Massachusetts Institute of Technology, Cambridge, MA 02139, USA.

[c]Materials Science Division, Lawrence Berkeley National Laboratory, Berkeley, CA 94720, USA.

[†]Present address: Department of Nuclear Science and Engineering, Massachusetts Institute of Technology, Cambridge, MA 02139, USA.

*email: raphjclem@gmail.com

Abstract

Fluorine substitution for oxygen in cation-disordered lithium-excess transition metal oxides ($Li_{1+x}TM_{1-x}O_2$) used as lithium-ion cathodes was recently demonstrated to improve the reversibility of the processes taking place on charge and discharge by reducing the amount of oxygen loss on charge and preventing major structural rearrangements at high voltage. Yet, little is understood about how fluorine incorporates the oxide structure and impacts its electrochemical properties. Here, we use a combination of experimental (solid-state Nuclear Magnetic Resonance (NMR) spectroscopy) and theoretical techniques (density functional theory (DFT) calculations and Monte Carlo simulations) to investigate the evolution of the local structure around fluorine and lithium, and the oxidation state of redox-active nickel during charge and discharge of the $Li_{1.15}Ni_{0.45}Ti_{0.3}Mo_{0.1}O_{1.85}F_{0.15}$ (LNF15) cathode. We show that fluorine doping introduces short-range order in as-synthesized LNF15, by incorporating in lithium-rich sites with five or six lithium nearest-neighbors. We observe the emergence of new signals in the *ex situ* ^{19}F NMR spectra taken at high states of charge, which we tentatively assign to undercoordinated, diamagnetic fluorine environments seen in our computed models. Our theoretical results also suggest that octahedral nickel ions directly bonded to fluorine follow a different oxidation mechanism than those surrounded by six oxygens, forming Ni^{3+} intermediates instead of oxidizing from Ni^{2+} directly to Ni^{4+}. While the oxidation of Ni^{2+} towards Ni^{4+} is incomplete in oxides, due to overlap between the oxygen and nickel valence states, this result suggests that fluorination may be an efficient strategy to utilize the Ni^{2+}/Ni^{4+} redox reservoir to a greater extent.

Introduction

The transition to renewable energy sources, the building of smart grids, and the electrification of transportation all rely on the development of high performance electrical energy storage technologies. Rechargeable batteries are modular and scalable, and as such can meet the demands of a wide range of applications. Despite ongoing research into various types of secondary batteries (e.g Li-S, redox flow, Na-, Mg- and K-ion batteries, to name a few), the Li-ion technology still dominates the market. Further performance improvements in this space rely in part on finding Li-ion positive electrodes with a higher energy density. Among candidate materials, Li-excess transition metal (TM) oxides with general formula $Li_{1+x}TM_{1-x}O_2$ are promising as they can deliver a high capacity at a high voltage, resulting in high energy density. It was recently demonstrated that, provided Li is more than 10% in excess ($x > 0.1$), $Li_{1+x}TM_{1-x}O_2$ compounds need not be perfectly layered structures (with alternating Li and TMO_2 layers within the rocksalt anion sublattice) but can instead exhibit a disordered cation lattice and still be percolating to Li^+ ions, greatly expanding the design space of potential transition metal oxide cathodes.[1,2]

Perhaps the main challenge faced by $Li_{1+x}TM_{1-x}O_2$ materials is the stabilization of the cathode surface structure at high voltage. While $Li_{1+x}TM_{1-x}O_2$ cathodes display a large first charge capacity with an electrochemical curve characterized by a long plateau at high voltage, the redox mechanisms and structural phenomena taking place close to the surface of the particles during this initial Li extraction process (charge) are not fully reversible on subsequent Li reinsertion (discharge), leading to gradual performance degradation that is a severe obstacle to commercialization.[3] Specifically, redox phenomena involving O^{2-} anions have been found to result in the loss of oxygen from the cathode structure - e.g., for Li-Ni-Ti-Mo-O_2 cathode materials, O_2 gas evolution is observed from ~4.35 V on charge[4] - and profound structural rearrangements including TM migration and the formation of a densified layer at the surface of the cathode particles.[5-8]

Fluorination of cation-disordered $Li_{1+x}TM_{1-x}O_2$ compounds was recently proposed as an effective way to reduce the amount of oxygen loss from the cathode compound on charge and to prevent irreversible

structural changes at high voltage. For example, we recently showed that the cation-disordered $Li_{1.15}Ni_{0.45}Ti_{0.3}Mo_{0.1}O_{1.85}F_{0.15}$ (LNF15) cathode material can be synthesized via a standard solid-state synthesis route.[4] When compared to its oxide counterpart, $Li_{1.15}Ni_{0.375}Ti_{0.375}Mo_{0.1}O_2$ (LN15), as-synthesized LNF15 contains more redox-active Ni^{2+} (as a result of substitution of O^{2-} by lower valent F^-), which leads to an increase in the TM redox reservoir and less oxygen oxidation on delithiation, so that a significant decrease in the amount of O_2 and CO_2 gas evolution is observed on charge to 4.6 V. As a result, LNF15 exhibits less polarization of its voltage curve, and a higher energy density and rate capability than LN15. These performance improvements have been ascribed to more reversible redox and structural processes taking place on cycling.[4] However, little is understood about how F substitution takes place and how it impacts the electrochemical properties of the oxide on a mechanistic level. In this work, we use a combination of experimental and theoretical techniques to investigate the impact of fluorination on the local structure and electrochemistry of the LNF15 cathode.

We rely on *ex situ* ^{19}F and ^{7}Li solid-state Nuclear Magnetic Resonance (ssNMR) to investigate the F and Li environments in the as-synthesized material and in cathode samples collected at different stages of charge and discharge. As a local probe of structure, NMR is particularly well suited for the study of amorphous or highly disordered materials, such as pristine and partially delithiated cathodes.[9] However, the presence of open-shell TM species in the material, here Ni^{2+} and Ni^{3+} formed on charge, leads to complex NMR spectra. The strong hyperfine (or paramagnetic) interaction between unpaired TM electrons and the nucleus under consideration results in large chemical shifts and broad resonances. The interpretation of the resulting spectra, composed of broad overlapping signals, can be greatly assisted by first principles calculations of NMR parameters.[10-13] Whilst a number of NMR studies of paramagnetic Li-ion and Na-ion layered oxide cathodes have been able to make clear assignments of the Li and Na environments in the interlayer space and in the TMO_2 layers,[14-19] the investigation of paramagnetic disordered rocksalt oxides is complicated by the intrinsic disorder on the cation lattice, leading to a great variety of local environments with similar shifts.[4,20] In these disordered structures, in addition to computed NMR shifts, an understanding of the distribution of local environments is crucial to interpret the NMR data. We obtain this distribution

from Monte Carlo (MC) simulations based on a cluster expansion (CE) Hamiltonian parametrized using density functional theory (DFT), which reveals the short-range ordering of the cations and the types of F and Li local environments present at different stages of delithiation. To the best of our knowledge, only one recent study has so far applied ^{7}Li NMR spectroscopy and MC simulations to investigate disorder in the as-prepared $Li[Ni_{1/3}Mn_{1/3}Co_{1/3}]O_2$ cathode.[21] Our work is the first instance of a combined NMR and CE/MC simulation study of a cathode material in the pristine state and at different stages of charge, giving important insight into the impact of fluorine substitution on the local cation order and properties of the LNF15 cathode.

In this article, we first investigate short-range order resulting from the introduction of F in the oxide lattice using CE/MC simulations and ^{19}F NMR of as-synthesized LNF15. We then explore the behavior of this material upon (de)lithiation, focusing on the influence of fluorination on the Ni oxidation mechanism, as well as on changes in the F local environments during cycling. Finally, we discuss the impact of F substitution on the electrochemical properties of LNF15.

Methods

Cluster expansion and Monte Carlo simulations

Representative structures of the fully lithiated $Li_{1.166}Ni^{2+}_{0.333}Ti_{0.5}O_{1.833}F_{0.166}$ material were obtained from Monte Carlo simulations based on a cluster expansion Hamiltonian. A cluster expansion parametrizes the internal energy of a system on a fixed lattice (here, dense rocksalt) across its configurational degrees of freedom using a sum of many-body interactions.[22] We constructed the cluster expansion using pair interactions up to 7.1 Å, triplet interactions up to 4.0 Å, and quadruplet interactions up to 4.0 Å based on a primitive rocksalt unit cell with lattice constant a = 3 Å, where the interactions are taken as an offset from a baseline of formal-charge electrostatics with a fitted dielectric constant.[23] To fit the strength of each interaction, we used an L_1-regularized least-squares regression, with the regularization parameter chosen to minimize cross-validation errors.[24] The out-of-sample root-mean-square error resulting from this procedure was 11 meV per atom. The fitting data for this regression consisted of the internal energies of 1301 orderings of Li^+, Ni^{2+}, Ti^{4+}, O^{2-}, and F^- on a rocksalt lattice across the LiF-NiO-Li_2TiO_3 space, computed

with density functional theory (DFT) using the projector-augmented wave (PAW) method[25] as implemented in the Vienna Ab-Initio Simulation Package (VASP)[26]. For these calculations, we relied on the PBE exchange-correlation functional[27] with the rotationally-averaged Hubbard U correction as previously calibrated for oxide materials (U = 6.0 eV for Ni[28]). All calculations were converged to 10^{-6} eV on total energy and 0.02 eV/Å on interatomic forces using a reciprocal space discretization of 25 $Å^{-1}$.

The Li-vacancy configurations appearing upon delithiation of $Li_{1.166}Ni_{0.333}Ti_{0.5}O_{1.833}F_{0.166}$ were obtained using a separate cluster expansion which takes into account Li-vacancy interactions, as well as the various oxidation states of Ni and O which appear on charge. Using the same interaction ranges as in the fully-dense rocksalt case, this cluster expansion was fitted using the energies of small unit-cell Li-vacancy orderings enumerated using the SCAN meta-GGA exchange-correlation functional,[29] as this functional has been reported to accurately reproduce structure selection[30,31]. Ground-state Li-vacancy orderings thus obtained at each delithiation level for each representative $Li_{1.166}Ni_{0.333}Ti_{0.5}O_{1.833}F_{0.166}$ structure were fully relaxed using the hybrid HSE functional[32] with an exact-exchange fraction of 0.30, calibrated to reproduce Ni oxidation behavior using single-shot G_0W_0 calculations[33]. For these calculations, the reciprocal space discretization was reduced to 10 $Å^{-1}$ to reduce computational expense.

To construct a representative voltage profile of the disordered $Li_xNi_{0.333}Ti_{0.5}O_{1.833}F_{0.166}$ material accounting for short-range order and the effects of F doping, we computed the Li chemical potential as a function of Li content in 32 representative structures of $Li_xNi_{0.333}Ti_{0.5}O_{1.833}F_{0.166}$, drawn at random from equilibrated Monte Carlo simulations on the fully lithiated equivalent mimicking the synthesis conditions. We then constructed a semi-grand-canonical ensemble of $Li_xNi_{0.333}Ti_{0.5}O_{1.833}F_{0.166}$ based on these Li potentials, yielding a statistically-averaged Li chemical potential, or equivalently, a delithiation voltage, at all states of charge. To determine the electronic configuration of each structure, we compare the magnetic moments of each atom to characteristic moments expected for various oxidation states, checking to ensure that the oxidation state assignments preserve charge neutrality. All structural analyses were performed using the pymatgen software package[34].

^{7}Li and ^{19}F solid-state NMR: Experimental details and dominant interactions

Details on the solid-state synthesis of $Li_{1.15}Ni_{0.375}Ti_{0.375}Mo_{0.1}O_2$ (LN15) and $Li_{1.15}Ni_{0.45}Ti_{0.3}Mo_{0.1}O_{1.85}F_{0.15}$ (LNF15) cathode powders can be found in earlier work.[4] The LNF15 cathode film was prepared using a 70:20:10 weight ratio of active material (LNF15) to carbon black (Timcal, Super C65) to polytetrafluoroethylene (PTFE, Dupont, Teflon 8A) binder. Charged and discharged samples for NMR characterization were obtained by assembling and cycling half-cells composed of the LNF15 film, 1 M $LiPF_6$ in a 1:1 volume ratio of ethylene carbonate (EC) and dimethyl carbonate (DMC) (BASF), Glass microfiber filters (Whatman), and Li metal foil (FMC), used as the cathode, electrolyte, separator, and counter electrode, respectively. The loading density of the cathode film was ~7 mg/cm^2. All cells were cycled at 20 mA/g of active material.

All ^{19}F and ^{7}Li NMR data were acquired at room temperature on a Bruker Avance 500 MHz (11.7 T) wide-bore NMR spectrometer, at Larmor frequencies of -470.6 MHz and -194.4 MHz, respectively. The data were obtained under 60 kHz magic angle spinning (MAS) using a 1.3 mm double-resonance probe. ^{19}F and ^{7}Li chemical shifts were referenced against lithium fluoride (LiF, $\delta(^{19}F)$ = -204 ppm and $\delta(^{7}Li)$= -1 ppm). ^{19}F spin echo spectra were acquired on LiF and LNF15 samples using a 90° RF pulse of 1.6 µs and a 180° RF pulse of 3.2 µs at 76.3 W. Recycle delays of 14 s and 50 µs were used for LiF and LNF15 samples, respectively. In addition, ^{19}F pj-MATPASS[35] (projected Magic-Angle Turning Phase-Adjusted Sideband Separation) isotropic spectra were acquired on LNF15 samples using a 90° RF pulse of 1.6 µs at 76.3 W and a recycle delay of 50 µs. A ^{19}F probe background spin echo spectrum, acquired under the same conditions as the spin echo spectrum of LNF15 samples but on an empty 1.3 mm rotor, revealed no significant background signal. The LiF ^{7}Li spin echo spectrum was acquired using a 90° RF pulse of 0.9 µs and a 180° RF pulse of 1.8 µs at 110 W and a recycle delay of 60 s. ^{7}Li pj-MATPASS isotropic spectra were acquired on LNF15 samples using a 90° RF pulse of 0.9 µs at 110 W and a recycle delay of 30 µs. Lineshape analysis was carried out using the SOLA lineshape simulation package within the Bruker Topspin software.

Although ^{7}Li is a spin-3/2 quadrupolar nucleus, its quadrupole moment is small and, in paramagnetic materials, the experimental ^{7}Li shift (δ_{exp}) is usually approximated to its dominant hyperfine term (δ_{para}): [13,19,36,37]

$$\delta_{exp}(^{7}\mathrm{Li}) = \delta_{para} \quad (1).$$

In contrast to ^{7}Li, ^{19}F is a spin-1/2 nucleus with a non-zero diamagnetic shift contribution (δ_{dia}) that can be of the same order of magnitude as the paramagnetic shift. The experimental ^{19}F shift is given by:

$$\delta_{exp}(^{19}\mathrm{F}) = \delta_{dia} + \delta_{para} \quad (2),$$

where δ_{dia}, for octahedral F in LNF15, is taken to be equal to the isotropic shift of octahedral F in diamagnetic LiF (-204 ppm).

Paramagnetic interactions come in two forms: isotropic Fermi contact interactions and anisotropic electron-nuclear dipolar couplings. Fermi contact interactions result in the delocalization of unpaired electron density from the transition metal *d* orbitals (here Ni) to the *s* orbital of the nucleus of interest (here ^{7}Li or ^{19}F), either through space or through bonds, giving rise to a Fermi contact shift (δ_{FC}) proportional to the unpaired spin density at the nuclear position, as derived by Kim et al.[11] The nuclear spin density can be obtained from first principles CRYSTAL calculations, as discussed below. Anisotropic through-space electron-nuclear dipolar interactions are only partially averaged out by fast spinning of the sample at the magic angle (MAS) and contribute to the intensity of the sideband manifold. When the magnetic susceptibility tensor is anisotropic, through-space electron-nuclear couplings result in a small pseudo-contact shift (δ_{PC}). Previous studies on similar materials have found that the pseudo-contact term is negligible compared to the Fermi contact term,[9,19] so that the overall paramagnetic shift is approximated here to the Fermi contact shift:

$$\delta_{para} = \delta_{FC} \quad (3).$$

Hybrid DFT/HF calculations of paramagnetic NMR parameters

Spin-unrestricted hybrid DFT/HF calculations were performed on $Li_{1.125}Ni^{2+}_{0.4375}Ti_{0.4375}O_{1.75}F_{0.25}$ and $Li_{1.125}Ni^{3+}_{0.875}O_{1.75}F_{0.25}$ cells used as model structures for the LNF15 compound at the beginning and at intermediate stages of charge. The CRYSTAL14 all-electron linear combination of atomic orbitals (LCAO) code[38] was used, and two spin-polarized exchange-correlation functionals based upon the B3LYP form were applied, with weights of Hartree-Fock (HF) exchange of 20% (B3LYP or H20) and 35 % (H35). Electron-nuclear hyperfine NMR parameters were obtained in ferromagnetically-aligned cells (at 0 K), using a method identical to that described elsewhere.[11,12] Briefly, the Fermi contact shift (δ_{FC}) is computed from the spin density at the nuclear position and the electron-nuclear dipolar anisotropy ($\Delta\delta$) is obtained from the principal components of the electron-nuclear dipolar tensor at the nucleus. Both δ_{FC} and $\Delta\delta$ are subsequently scaled to values consistent with the room temperature paramagnetic state in which the experiments are performed by multiplication by the so-called magnetic scaling factor Φ:[11]

$$\Phi(\mathrm{T}) = \frac{B_0 {\mu_{\mathrm{eff}}}^2}{3k_{\mathrm{B}} g_{\mathrm{e}} \mu_{\mathrm{B}} S(\mathrm{T} - \Theta)} \quad (4),$$

where B_0 is the external magnetic field strength; μ_{eff}, the effective magnetic moment per Ni site; k_{B}, Boltzmann's constant; g_e, the electron g-factor; μ_B, the Bohr magneton; S, the average spin per transition metal site; T, the temperature of the sample (assumed equal to 320 K to account for frictional heating caused by fast (60 kHz) rotation of the NMR rotor); and Θ, the Weiss constant obtained from magnetic susceptibility measurements on as-synthesized LNF15. Full details of the calculations, including the basis sets and numerical parameters, are presented in the Supplementary Information.

Reconstruction of the ^{19}F NMR spectra of pristine LNF15

The ^{19}F NMR spectrum of pristine LNF15 was reconstructed at 673 K, 973 K, 1273 K and in the infinite temperature limit (10^8 K) using the distribution of F environments determined from MC simulations on the model $Li_{1.166}Ni_{0.333}Ti_{0.5}O_{1.833}F_{0.166}$ structure. The spectra were obtained in MATLAB by adding a series of normal probability distribution functions with position and width equivalent to the shifts and static (0 K) paramagnetic broadening of the signals corresponding to the various F environments in the structure, as determined from NMR calculations.

Magnetic susceptibility measurements

The field cooled (FC) and zero field cooled (ZFC) DC magnetic susceptibility of as-synthesized LNF15 and LN15 was recorded on a commercial magnetic property measurement system (MPMS), over the temperature range 2 to 390 K and under an external field of 1000 Oe.

Results

Short-range order in the pristine LNF15 cathode material

Fluorination is a widely-used strategy to improve the thermal and electrochemical stability of various components of secondary batteries. For instance, the introduction of highly electronegative F into organic solvents lowers the highest occupied molecular orbital (HOMO) level, leading to an increase in the oxidation potential. Hence, electrolytes with a high voltage stability are often prepared using a fluorinated electrolyte salt (e.g. $LiPF_6$) and solvent (e.g. fluoroethylene carbonate or FEC). In addition, insulating fluorinated compounds are used as coatings and enhance the stability of cathode materials by inhibiting exothermic reactions between the cathode surface and the electrolyte on charge. On the other hand, F substitution for O in the bulk of layered transition metal oxides has proved extremely challenging, and previous reports have found that the LiF precursor is instead deposited as a thin layer at the surface of the oxide cathode particles.[39,40] A recent theoretical study demonstrated that stoichiometric layered oxides

($LiTMO_2$) are expected to be extremely difficult to fluorinate because of the high formation energy of TM-F bonds. Unlike layered $LiTMO_2$ compounds, Li-excess layered or cation-disordered $Li_{1+x}TM_{1-x}O_2$ materials contain metal-poor/Li-rich anion sites that enable small amounts of F to incorporate into the oxide structure.[41] LNF15 is a good example of this new class of cation-disordered rocksalt cathodes, with about 7.5 % of O replaced by F.[4] In this section, CE/MC simulations are combined with ^{19}F solid-state NMR to investigate short-range order in the as-synthesized LNF15 cathode by directly probing the F local environments.

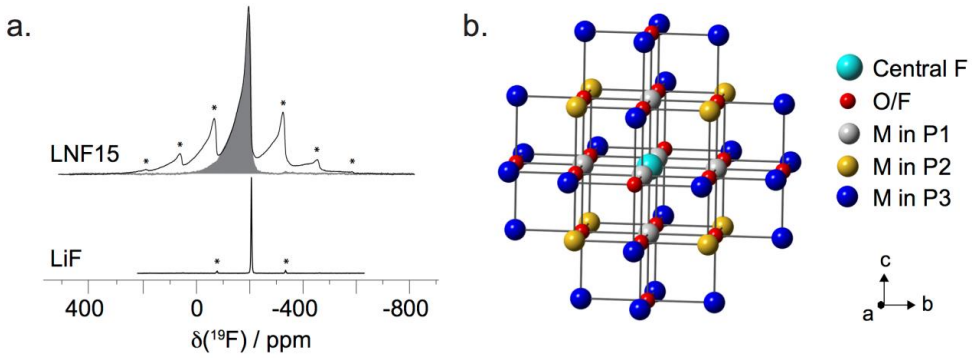

Figure 1. (a) ^{19}F spin echo NMR spectra obtained on as-synthesized $Li_{1.15}Ni_{0.45}Ti_{0.3}Mo_{0.1}O_{1.85}F_{0.15}$ (LNF15) and LiF powders at 60 kHz magic angle spinning (MAS). Spinning sidebands in the spin echo spectra are indicated with asterisks. The ^{19}F projected magic angle turning phase-adjusted sideband separation (pj-MATPASS) isotropic spectrum collected on LNF15 is shown with a grey shading. (b) Typical F local environment in a rocksalt transition metal oxyfluoride compound, including the first three metal coordination shells (P1, P2 and P3) around the central F atom.

While solid-state NMR has been widely applied to study alkali environments (e.g. Li, Na) in paramagnetic transition metal oxide cathodes, it has seldom been used to investigate anion sites, partly because anions are directly bonded to the TM, resulting in very strong hyperfine interactions. For pure oxides, NMR-active ^{17}O has a low natural abundance (0.037%) and a large nuclear quadrupole moment that leads to very broad, low intensity signals that are difficult to interpret. A recent report on paramagnetic ^{17}O NMR of ^{17}O-enriched Li_2MnO_3 suggests, however, that this technique may be applied to a wider range of materials.[42] ^{19}F is an ideal candidate for NMR spectroscopy, owing to its 100 % natural abundance and a

nuclear spin *I=1/2* (i.e. no quadrupolar interactions), meaning that anion sites can more easily be probed in transition metal oxyfluorides.

^{19}F NMR spectra obtained on LNF15 and LiF powders are shown in Figure 1a. The LiF spectrum is composed of a single resonance at -204 ppm corresponding to the unique diamagnetic F site in the structure. This signal is also present in the much broader spin echo spectrum obtained on the as-synthesized cathode powder, suggesting that LiF-like environments are present in the oxyfluoride. The isotropic projected-MATPASS[35] spectrum collected on LNF15 (in which spinning sidebands are suppressed, allowing direct determination of the chemical shifts) and shown with a grey shading is composed of broad, overlapping signals spanning a wide range of resonant frequencies. Hence, there are a number of additional F environments in LNF15, which confirms that F has integrated the bulk oxide lattice and is consistent with our previous study.[4] Both signal broadening and a shift of the resonant frequency away from -204 ppm are evidence for paramagnetic interactions between the F nuclei and unpaired Ni^{2+} electrons in LNF15. A more detailed assignment of the ^{19}F spectrum obtained on as-synthesized LNF15 requires knowledge of the overall shift and linewidth of the F signals due to the various F environments in the cation-disordered cathode, as well as the relative population of these environments.

As mentioned in the methods section, the paramagnetic shift can be approximated by the Fermi contact shift (see eq. (3)) proportional to the unpaired spin density transferred from the Ni *d* orbitals to the F *s* orbital either directly through space or via through-bond spin density transfer pathways. Fermi contact interactions are short-range (typically < 5 Å) and Ni centers beyond the first three metal coordination spheres around the central F, depicted in Figure 2b, are not expected to contribute significantly to the overall shift. In addition, Fermi contact shifts are additive, so that the total Fermi contact shift of the central F site in Figure 2b is the sum of individual contributions from Ni ions in positions P1 (directly bonded to F), P2 (second metal shell) and P3 (third metal shell). Hence, if P1-, P2- and P3-type shift contributions are known, the total paramagnetic shift of a F site with an arbitrary number of Ni ions in its first, second and third metal shells can be reconstructed, helping the assignment of the experimental data. Individual Fermi contact shift contributions can be obtained from first principles using the 'spin-flipping' technique devised by

Middlemiss et al.[12] For example, the shift contribution from a Ni directly bonded to F (P1-type contribution) is obtained from the difference between the unpaired spin density at the F nucleus computed in a ferromagnetically-aligned cell (all Ni 'spin up'), and that computed in a cell where the spin of one Ni in P1 is flipped (all other spins are still 'spin up'). The technique is then repeated for Ni ions in P2 and P3 to obtain all possible types of contributions. Here, to gain insight into the possible paramagnetic F environments present in as-synthesized and electrochemically-cycled LNF15 samples, P1, P2 and P3 Ni^{2+} and Ni^{3+} contributions were obtained on $Li_{1.125}Ni^{2+}_{0.4375}Ti_{0.4375}O_{1.75}F_{0.25}$ and $Li_{1.125}Ni^{3+}_{0.875}O_{1.75}F_{0.25}$ structures, respectively, sampled from Monte Carlo simulations utilizing the cluster expansions described here and in our previous report[41]. Two hybrid DFT functionals with 20% (H20) and 35% (H35) Hartree-Fock exchange were employed, as explained in the methods section, and the results are presented in Table 1. Our calculations predict that each Ni in the first coordination shell around F adds a ca. 5500 ppm shift to the overall resonant frequency, whereas the shift contributions for Ni ions in the second and third metal shell are comprised between -28 and +22 ppm.

Interaction type	Ni^{2+}		Ni^{3+}	
	$\delta(H20)$ / ppm	$\delta(H35)$ / ppm	$\delta(H20)$ / ppm	$\delta(H35)$ / ppm
P1	5548	5494	5537	5998
P2	-28	-26	-5	-2
P3	15	10	22	13

Table 1. Individual Ni^{2+} and Ni^{3+} P1-, P2- and P3-type Fermi contact contributions to the overall ^{19}F paramagnetic shift obtained from hybrid DFT/HF calculations on $Li_{1.125}Ni^{2+}_{0.4375}Ti_{0.4375}O_{1.75}F_{0.25}$ and $Li_{1.125}Ni^{3+}_{0.875}O_{1.75}F_{0.25}$ structures using the H20 and H35 functionals (containing 20 and 35% Hartree-Fock exchange, respectively) and a magnetic scaling factor $\Phi = 0.02375$ as described in the Supporting Information. Due to the large number of possible bond pathway interactions (e.g. F-Ni-O-Ni vs. F-Li-O-Ni for P2-type Ni…F interactions), the shift contributions listed in this table are averages over all values obtained for a specific pathway type (P1, P2 or P3).

The main source of broadening of the ^{19}F NMR signals comes from the paramagnetic interactions with nearby Ni ions in the LNF15 material. The paramagnetic broadening of a F signal in a static sample (i.e. no spinning at the magic angle) at 0 K is equal to the hyperfine dipolar anisotropy ($\Delta\delta$, in ppm) of the corresponding F environment, which can be extracted from our NMR calculations. Average $\Delta\delta$ values for

F environments with zero, one and two Ni in the first coordination shell in the $Li_{1.125}Ni^{2+}_{0.4375}Ti_{0.4375}O_{1.75}F_{0.25}$ and $Li_{1.125}Ni^{3+}_{0.875}O_{1.75}F_{0.25}$ model structures are summarized in Table 2. The computed $\Delta\delta$ values reveal that NMR signals from F nuclei with no Ni nearest-neighbor are a lot sharper ($\Delta\delta$ ~ 300 ppm) than those from F nuclei with at least one Ni in the first coordination shell ($\Delta\delta$ ~ 5000-6000 ppm). In addition, $\Delta\delta$ values for F sites with one or two Ni^{3+} nearest-neighbors are fairly similar, suggesting that the first nearest-neighbor Ni broadens the F resonance significantly while additional nearest-neighbor Ni ions do not lead to significant further signal broadening.

	Ni^{2+}		Ni^{3+}	
	$\lvert\Delta\delta\rvert(H20)$ / ppm	$\lvert\Delta\delta\rvert(H35)$ / ppm	$\lvert\Delta\delta\rvert(H20)$ / ppm	$\lvert\Delta\delta\rvert(H35)$ / ppm
0 Ni in P1	286	296	243	279
1 Ni in P1	5240	4874	5960	5724
2 Ni in P1	--	--	5574	5432

Table 2. Average electron-nuclear dipolar anisotropy parameters, $\Delta\delta$ (in ppm), for F environments with zero, one and two Ni in the first coordination shell in the $Li_{1.125}Ni^{2+}_{0.4375}Ti_{0.4375}O_{1.75}F_{0.25}$ and $Li_{1.125}Ni^{3+}_{0.875}O_{1.75}F_{0.25}$ model structures, as obtained from first principles calculations using the H20 and H35 hybrid functionals and a magnetic scaling factor $\Phi = 0.02375$ as described in the Supporting Information.

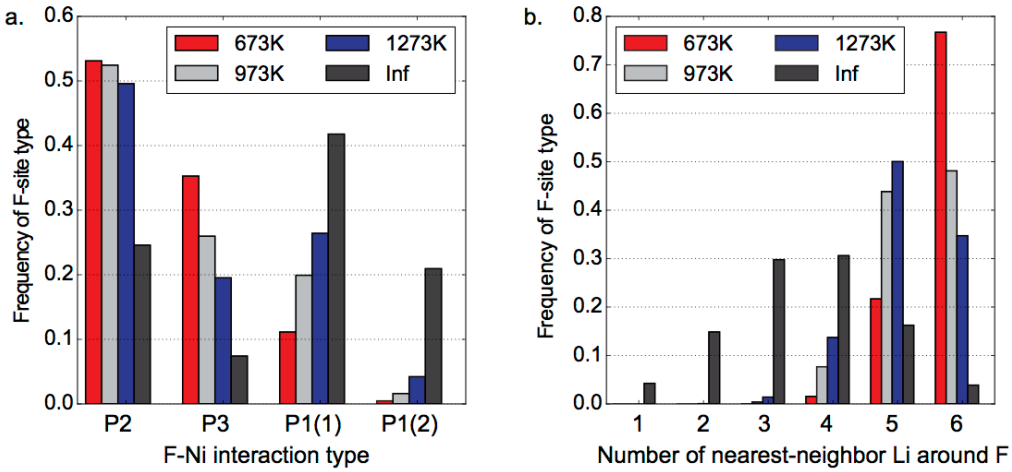

Figure 2. Distribution of F environments in the simulated $Li_{1.166}Ni_{0.333}Ti_{0.5}O_{1.833}F_{0.166}$ material as a function of Monte Carlo equilibration temperature, where "Inf" corresponds to 10^8 K as a model of the infinite temperature limit. F sites are distinguished by (a) the number of Ni ions in the first (P1), second (P2) and third (P3) cation coordination shell or, (b) the number of nearest-neighbor Li around the F atom. The distribution of F sites across F-Ni environments shown in (a) is split into four environments capturing the majority of F sites in the material: P1(1), corresponding to 1 nearest-neighbor Ni; P1(2), corresponding to 2 nearest-neighbor Ni; P2, corresponding to 0 nearest-neighbor Ni and at least 1 Ni in the second cation-

neighbor shell; P3, corresponding to 0 Ni in the first two cation neighbor shells and at least 1 Ni in the third cation-neighbor shell.

The distribution of F local environments in $Li_{1.166}Ni_{0.333}Ti_{0.5}O_{1.833}F_{0.166}$ obtained from large-cell MC simulations across a range of simulated annealing temperatures and in the random (infinite temperature) limit is presented in Figure 2. We choose the $Li_{1.166}Ni_{0.333}Ti_{0.5}O_{1.833}F_{0.166}$ composition as a model of LNF15 as it contains a representative Li-to-metal ratio and fluorine content, the two compositional features critical to understanding fluorine incorporation into a disordered rocksalt transition metal oxide.[41] F environments are classified according to the number of Ni ions in their first, second and third cation coordination shells in Figure 2a, and according to the number of nearest-neighbor Li^+ ions in Figure 2b. Differences in the distributions of F environments in the random limit, labeled as "Inf" in the figure, and in the 973 K case, representative of the annealing temperature used in the LNF15 synthesis, reveal that short-range order is clearly present in the as-synthesized cathode. The short-range order repels Ni from the F and instead creates Li-rich nearest-neighbor environments around F, consistent with the much larger formation energy of TM-F bonds, as compared to Li-F bonds.[41] The Ti-F interaction is similarly high in energy, reducing the population of Ti-F bonds. Correspondingly, we find that half of the F are 6-fold coordinated by Li, even within the F solubility limit, and less than half of the remaining F have any Ni in the P1 shell. These computed distributions, put together with the NMR parameters computed earlier, allow for an analysis of the F sites detected with ^{19}F NMR spectroscopy.

Shown in Figure 3 are the reconstructed ^{19}F static NMR spectra, as obtained from the shifts and static paramagnetic broadening of the various F signals (from NMR calculations, see Tables 1 and 2) and from the distribution of F environments in the model $Li_{1.166}Ni_{0.333}Ti_{0.5}O_{1.833}F_{0.166}$ structure at different temperatures (from MC simulations, see Figure 2). Further details on the reconstruction procedure are provided in the methods section.

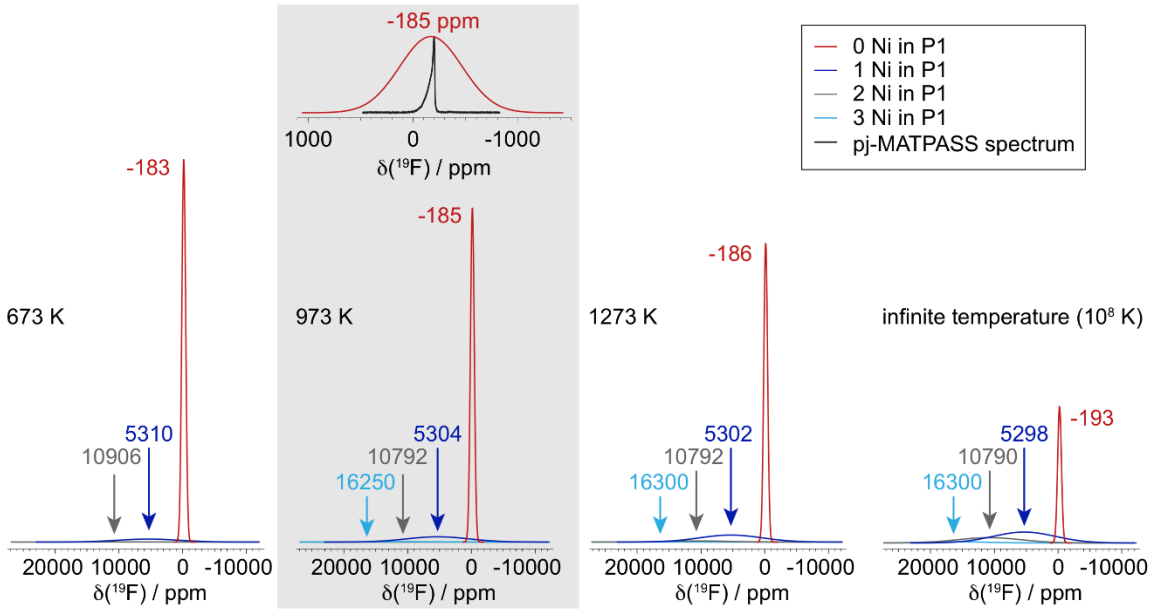

Figure 3. Reconstructed ^{19}F static NMR spectra for pristine LNF15 at 673 K, 973 K, 1273 K and at infinite temperature (10^8 K). The spectra were reconstructed using the distribution of F environments in $Li_{1.166}Ni_{0.333}Ti_{0.5}O_{1.833}F_{0.166}$ obtained from a large-cell MC simulation at the temperature of interest, the overall NMR shift computed for each F site in the structure, and the 0 K static paramagnetic broadening determined from first principles CRYSTAL calculations. NMR signals corresponding to F nuclei surrounded by zero, one, two or three nearest-neighbor Ni are depicted in red, green, purple and blue, respectively, and the resonant frequency corresponding to the maximum intensity of each signal is indicated on the spectra. A comparison of the experimental pj-MATPASS isotropic spectrum obtained on pristine LNF15 (synthesized at 700-750°C) and the reconstructed NMR spectrum at 973 K is shown in the shaded area.

The total ^{19}F NMR shift, for each F site present in the material, was obtained by summing over the diamagnetic and paramagnetic shift contributions (see eq. (2) and details in the methods section). The former was taken to be equal to the isotropic shift of octahedral F in diamagnetic LiF (-204 ppm), while the latter was computed by summing over all individual paramagnetic shift contributions from Ni ions in P1, P2 and P3 positions around the F nucleus under consideration. Since the F site distribution at 973 K is most representative of the actual distribution of F environments in LNF15 synthesized between 700 and 750°C, the 973 K static spectrum is compared to the experimental pj-MATPASS isotropic spectrum obtained on pristine LNF15 in Figure 3. We find that the experimental ^{19}F NMR signals lie within the frequency range expected for F sites with no Ni in P1. The overall experimental lineshape is a lot sharper than the static signal expected for the collection of F environments with no nearest-neighbor Ni in the material, likely

because of partial averaging of the anisotropic electron-nuclear interactions in the experimental sample as a result of 1) fast (60 kHz) spinning of the sample at the magic angle and 2) atomic motion at the experimental temperature (ca. 320 K). Although multiple NMR measurements were carried out at various excitation frequencies, from -4000 ppm to 10000 ppm in steps of 2000 ppm, no signal was observed in the 5000 to 10000 ppm range, where signals from F nuclei with one and two Ni nearest-neighbors are expected. Our MC simulations indicate, however, that there should be a significant number of F nuclei with at least one Ni in P1 at 973 K (see Figure 2). These results suggest that the resonances of F nuclei surrounded by at least one nearest-neighbor Ni are too broad to be observed and are lost in the background noise. Hence, our ^{19}F NMR data cannot be used to quantify the amount of F incorporated in the lattice of LNF15.

Overall, MC simulations on the model $Li_{1.166}Ni_{0.333}Ti_{0.5}O_{1.833}F_{0.166}$ structure suggest that there is a drive for short-range ordering around the F nuclei incorporated in the bulk LNF15 structure at the synthesis temperature (ca. 973 K). ^{19}F NMR data confirm the presence of paramagnetic F nuclei in pristine LNF15 with six diamagnetic metals (either Li^+, Ti^{4+} or Mo^{6+}) in the first coordination shell (P1) and Ni ions in the second and/or third coordination shells (P2 and P3). The smaller number of F nuclei with one Ni nearest-neighbor, as suggested from MC simulations, are invisible by NMR because of the very strong Ni-F paramagnetic interaction leading to extremely broad signals that are lost in the background noise. Finally, the magnetic susceptibility data obtained on the LN15 ($Li_{1.15}Ni_{0.375}Ti_{0.375}Mo_{0.1}O_2$) oxide and the LNF15 ($Li_{1.15}Ni_{0.45}Ti_{0.3}Mo_{0.1}O_{1.85}F_{0.15}$) oxyfluoride, presented in Figure S1 in the Supporting Information, confirm that both compounds are paramagnetic. However, the much larger Weiss constant obtained for the fluorinated compound ($\Theta = -305 \pm 1$ K), as compared with the oxide ($\Theta = -120 \pm 1$ K), indicates stronger Ni-Ni magnetic couplings in the former material. The stronger Ni-Ni interactions may result from the larger Ni content in LNF15, but they may also reflect the presence of short-range structural order leading to the formation of Ni clusters away from the F dopant ions.

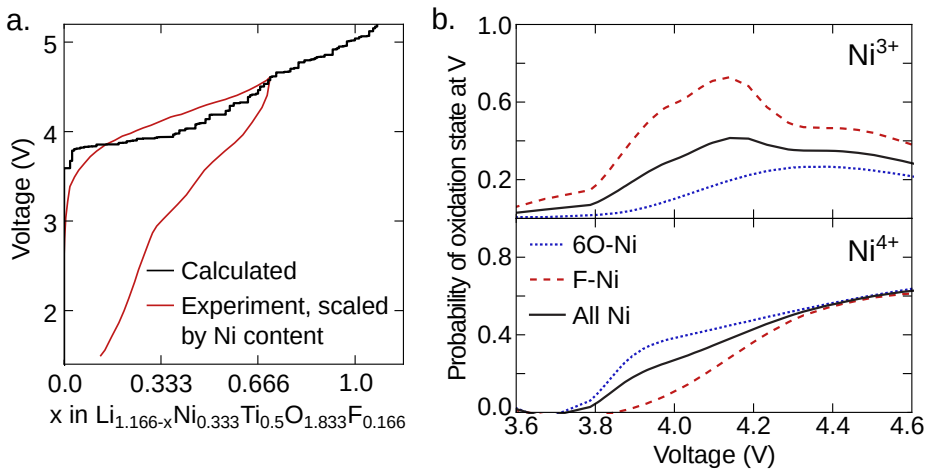

Figure 4. Computed oxidation mechanism for the disordered-rocksalt $Li_{1.166-x}Ni_{0.333}Ti_{0.5}O_{1.833}F_{0.166}$ system. (a) The computed voltage curve compared to the experimental first cycle voltage curve obtained on S-LNF15, where the experimental data have been scaled according to the Ni content (0.333 in $Li_{1.166-x}Ni_{0.333}Ti_{0.5}O_{1.833}F_{0.166}$ versus 0.45 in LNF15). (b) The probability of Ni^{3+} and Ni^{4+} formation as a function of voltage: at any given Ni site in the structure (black solid line), at Ni sites coordinated by 6 oxygen (dotted blue line), and at Ni sites with at least one nearest-neighbor F (dashed red line). All Ni sites sampled here are obtained from the fully relaxed structures used to compute the voltage curve in (a). Oxidation state assignments are made on the basis of magnetic moments in the fully-relaxed structures.

Electrochemical properties and local environments formed on Li (de)intercalation

Having established a model of as-synthesized LNF15, a key question to address is how fluorine incorporation in this material affects the electrochemical behavior. We begin this analysis using first-principles calculations of Li potentials in the $Li_{1.166-x}Ni_{0.333}Ti_{0.5}O_{1.833}F_{0.166}$ model system across a sample of representative $Li_{1.166}Ni_{0.333}Ti_{0.5}O_{1.833}F_{0.166}$ structures, as discussed in the methods section. The computed voltage curve for this system is shown in Figure 4a in comparison to the experimentally-obtained first-cycle voltage profile of shaker-milled LNF15 (S-LNF15). In this comparison, the experimental capacity is scaled by a factor of 0.333/0.45 so as to match the Ni content of S-LNF15 to that of $Li_{1.166}Ni_{0.333}Ti_{0.5}O_{1.833}F_{0.166}$ (0.45 and 0.333 per formula unit, respectively). This scaling is appropriate under the assumption that the voltage profile in this early region of the voltage curve is controlled by the Ni oxidation potential, rather than by Li-vacancy interactions, which is reasonable given the significantly higher voltage at the beginning of charge in this Ni-based system, as compared to that in disordered rocksalt cathodes based on other transition metals.[1,20,43,44] The agreement between the computed and scaled experimental voltage curve lends

further support to this assumption and suggests that the ensemble of partially delithiated structures underlying the derivation of the voltage curve provides a detailed sampling of the distribution of structures and oxidation states at different stages of charge.

Figure 4b depicts the probability that a Ni ion oxidizes to Ni^{3+} or Ni^{4+} as a function of voltage and its local anion environment, where the population of Ni^{2+}, Ni^{3+} and Ni^{4+} ions is sampled from all the Ni ions contained in the fully relaxed $Li_{1.166-x}Ni_{0.333}Ti_{0.5}O_{1.833}F_{0.166}$ structures appearing in the voltage curve in Figure 4a. The probability of any Ni oxidizing to Ni^{3+} or Ni^{4+}, regardless of anion environment, is represented by the 'All Ni' black line in Figure 4b, which indicates that Ni^{3+} and Ni^{4+} concurrently appear starting from 3.8 V. While the probability of observing Ni^{3+} peaks near 4.2 V, that of Ni^{4+} continues to rise, reaching a maximum of ~60% at 4.6 V. Comparing this value to the voltage curve in Figure 4a, 4.6 V corresponds to x~0.666 in $Li_{1.166-x}Ni_{0.333}Ti_{0.5}O_{1.833}F_{0.166}$, matching the theoretical $Ni^{2+/4+}$ capacity. Because only ~60% of the Ni oxidizes to Ni^{4+} at this voltage, some of the remaining oxidation must be accounted for by oxygen activity, in agreement with previous reports of oxygen redox appearing in competition with $Ni^{2+/4+}$ redox in both LN15 and LNF15.[4,8] We note that even upon further delithiation beyond 4.6 V, the probability of observing Ni^{4+} among all Ni in the structure never exceeds 60%, in agreement with previously reported x-ray absorption spectroscopy (XAS) results indicating that, in these disordered rocksalt cathodes, Ni is never fully oxidized to Ni^{4+}.

To understand the possible impact of F substitution on the mechanism of Ni oxidation, we further examine the probability of observing Ni^{3+} and Ni^{4+} at a given voltage: 1) at Ni sites featuring at least one Ni-F bond (the 'F-Ni' dashed red line in Figure 4b), and 2) at Ni sites coordinated only by oxygen (the '6O-Ni' dotted blue line in Figure 4b). Among '6O-Ni' sites, the probability of observing Ni^{3+} remains very low at all voltages, with a sharply increasing probability of Ni^{4+} formation starting at 3.8 V. Conversely, among 'F-Ni' sites, the probability of observing Ni^{4+} is suppressed at lower voltages and replaced by an increase in the probability of Ni^{3+} formation starting at 3.8 V. The probability of Ni^{4+} formation among both fluorinated and non-fluorinated Ni sites converges above 4.3 V, but the population of Ni^{3+} remains elevated among fluorinated Ni sites over that of purely oxygen-coordinated Ni environments. These data suggest

that fluorination promotes the formation of Ni^{3+} during Ni oxidation, changing the oxidation mechanism from direct Ni^{2+} -> Ni^{4+} oxidation in the pure oxide case, to Ni^{2+} -> Ni^{3+} -> Ni^{4+} in the oxyfluoride case. Equivalently, fluorination appears to suppress the $2Ni^{3+}$ -> Ni^{2+} + Ni^{4+} disproportionation reaction, which has been previously reported at low-temperature in Ni^{3+}-containing oxides both computationally and experimentally.[45-47]

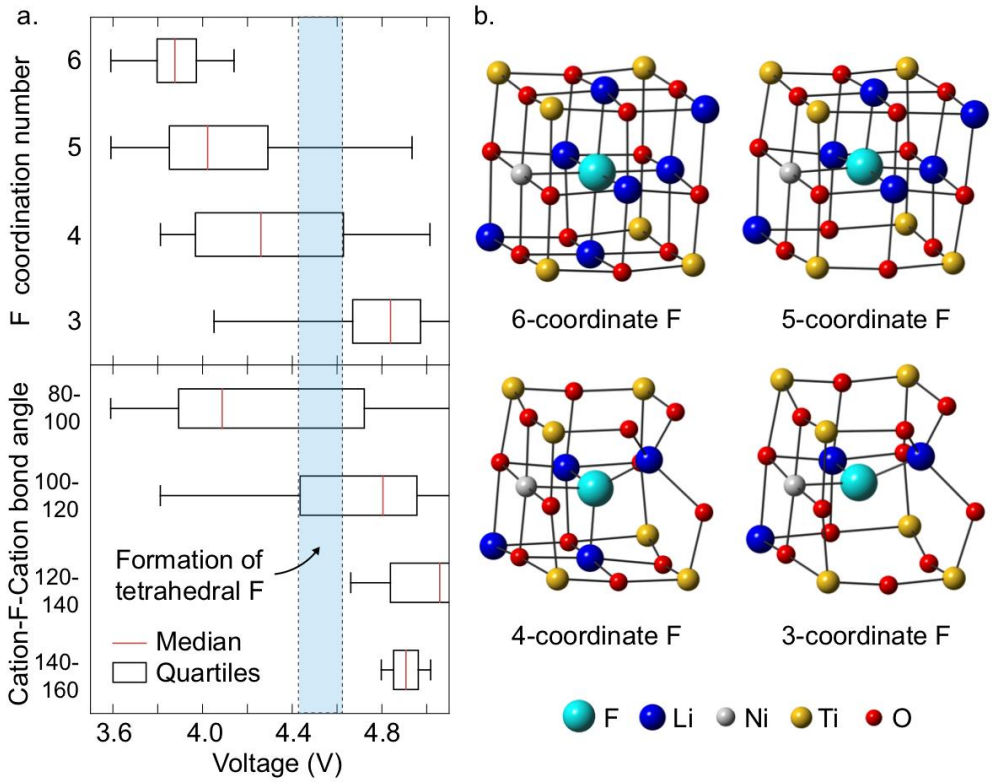

Figure 5. Distribution of F environments in the disordered-rocksalt $Li_{1.166-x}Ni_{0.333}Ti_{0.5}O_{1.833}F_{0.166}$ system as a function of voltage. (a) F environments are classified according to their coordination number in the upper panel, and according to their average cation-F-cation bond angle in the lower panel. For a given type of F environments, the median voltage at which it is observed is indicated with a red line, the full voltage range over which it is present is depicted with a black line, and the region delimited by the 25% and 75% quartiles of that voltage range is enclosed in a black box. Representative six-, five-, four- and three-coordinate F environments are depicted in (b). All F sites sampled here are obtained from the fully relaxed structures used to compute the voltage curve shown in Figure 4a.

Finally, Figure 5 shows the distribution of F local environments present in the delithiated $Li_{1.166-x}Ni_{0.333}Ti_{0.5}O_{1.833}F_{0.166}$ structures as a function of voltage. The upper panel of the figure shows the distribution of F environments classified according to their coordination number. Since most F anions are

surrounded by 6 and 5 Li in the first coordination shell in the pristine material (see Figure 2b), Li deintercalation leads to the formation of undercoordinated F on charge, as previously observed in Li-excess cation-disordered Li-Mn-V-O-F compounds.[53] Indeed, while all F species are surrounded by 6 cations below 3.9 V, they become five- and four-coordinated at higher potentials. In the 4.0-4.6 V range, for instance, most F are in four-coordinate environments. These environments could indicate the formation of two cation vacancies around a generally octahedral F or the migration of F from its initial octahedral site to an adjacent tetrahedral site. To distinguish between these two scenarios, we examine the distribution of F environments as a function of voltage, where this time F sites are classified according to their average cation-F-cation bond angle, as shown in the lower panel of Figure 5. F remaining in an octahedral-type site would be characterized by cation-F-cation bond angles in the 80-100° range (90° for adjacent cations in a perfect octahedron). A tetrahedrally-coordinated F would in turn be characterized by cation-F-cation bond angles in the 100-120° range (109.5° for a perfect tetrahedron). Based on the computed bond angles, we find that the 4.1-4.4 V voltage range is best characterized by octahedral F with 2 adjacent cation vacancies, while the 4.4-4.6 V range is best characterized by tetrahedral F.

With these insights in mind, we applied ^{19}F NMR to monitor changes in the local F environments in the bulk and at the surface of LNF15 particles during cycling by studying *ex situ* cathode films (composed of 70 %wt. active material, 20 %wt. carbon black, and 10 %wt. polyfluoroethylene (PTFE)) extracted at different stages along the first electrochemical cycle. The cycled cathode films were washed with DMC prior to the NMR experiments. We note that both ^{31}P and ^{7}Li NMR experiments were also performed on the cycled materials to gain further insight into the reactions taking place on cycling and assist the interpretation of the ^{19}F data. However, in the case of ^{31}P NMR, the signal from the 4.6 V charge LNF15 sample investigated was too weak to be detected. The ^{7}Li pj-MATPASS isotropic spectra collected on LNF15 samples at various stages of charge are compared to those obtained on pure oxide LN15 samples at similar potentials in Figure S2 and further discussed in the Supporting Information. Briefly, the combination of cation disorder in the material, leading to a large number of Li environments with similar shifts, and

paramagnetic interactions, broadening the Li resonances, results in very broad spectra which provide limited information on the processes occurring on Li extraction and involving F.

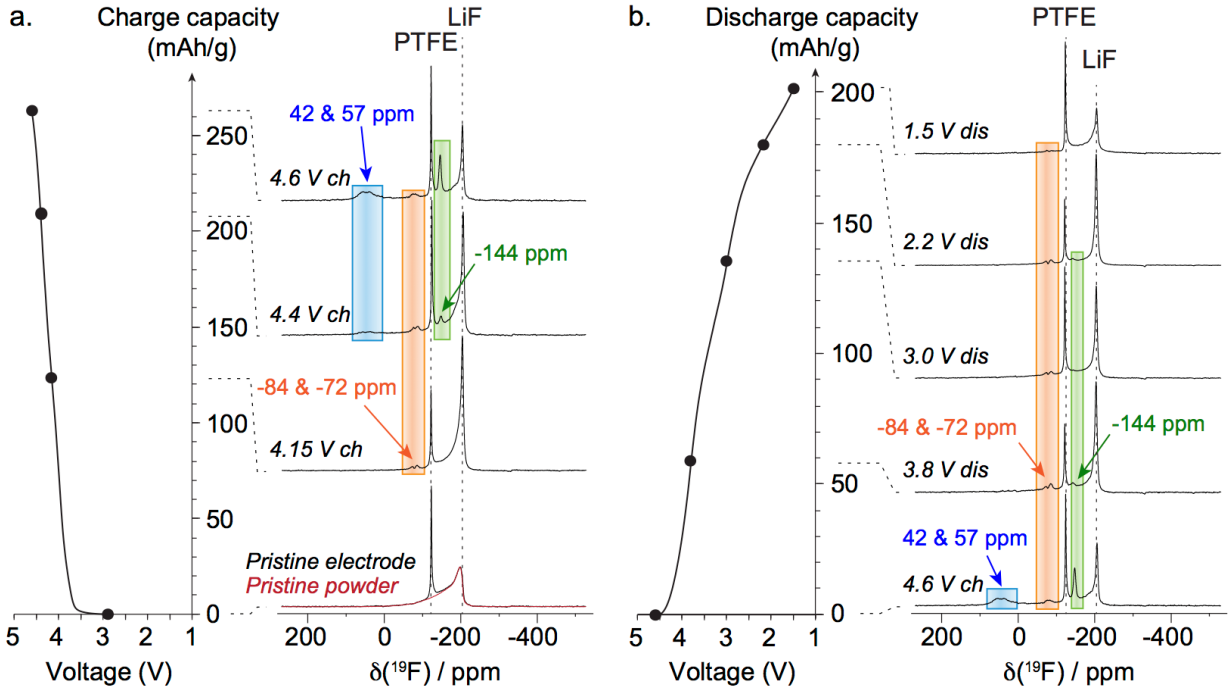

Figure 6. ^{19}F projected-MATPASS NMR spectra obtained at different stages along the first a) charge and b) discharge of LNF15. The points at which the cells were stopped and the cathode material was extracted for *ex situ* analysis are indicated on the electrochemical curves projected on the left of the spectra. LiF-like and PTFE signals at -204 and -121 ppm, respectively, are indicated by vertical dotted lines, while ^{19}F environments appearing on cycling are enclosed in yellow, blue and green rectangles.

The isotropic ^{19}F pj-MATPASS spectra obtained on charge and discharge are presented in Figures 6a and 6b, respectively. For the pristine composition, the spectra obtained on the powder sample and on the electrode film are overlaid. The ^{19}F signal from PTFE at -121 ppm is clearly observed in all cathode films, while the LiF-like ^{19}F signal at -204 ppm is more clearly observed in the cycled samples, which may indicate the formation of LiF in the solid electrolyte interface (SEI) layer at the surface of the cathode particles after contact with the electrolyte (1 M $LiPF_6$ in a solvent mixture of ethylene carbonate (EC) and dimethyl carbonate (DMC)). Both PTFE and LiF-like signals are indicated with dashed vertical lines in the spectra.

As discussed in the previous section, the broad signals around -160 to -190 ppm are due to F nuclei in the bulk LNF15 lattice with no nearest-neighbor Ni. Although Ni is oxidized on charge, these broad

signals do not change significantly up to 4.6 V. In fact, P2- and P3-type paramagnetic shift contributions are small and fairly similar for Ni^{2+} and Ni^{3+}, as shown in Table 1, and closed-shell Ni^{4+} (low spin d^6) does not contribute to the paramagnetic shift at all. Hence, the presence of either Ni^{2+}, Ni^{3+} or Ni^{4+} in P2 and in P3 should not impact the overall F resonant frequency significantly, explaining the small changes in the paramagnetic signals observable by NMR upon Li removal. The lower intensity of these broad signals in the spectrum obtained after one full charge/discharge cycle, as compared with the pristine spectrum, suggests fewer F environments with no Ni nearest-neighbor in the material after one cycle.

Several new signals appear on cycling and are highlighted in orange, blue and green in the spectra. Based on previous ^{19}F NMR studies of the SEI layer formed at the surface of transition metal oxide cathodes, the orange peaks at -72 and -84 ppm are assigned to F in the PF_6^- electrolyte salt and its decomposition products formed on charge, respectively.[48-50] On the other hand, the signals at 42 and 57 ppm (in blue), and at -144 ppm (in green) do not match any F signal reported for typical SEI phases. These signals are only present at high voltage and indicate the formation of new F environments either at the surface or in the bulk of the particles. ^{19}F pj-MATPASS isotropic spectra collected on the 4.6 V charge sample before and after air exposure, compared in Figure S2 in the Supporting Information, reveal that the broad signals at 42 and 57 ppm disappear after a few minutes of exposure to ambient air and moisture and are replaced by a sharp environment at 177 ppm, while the sharp green signal at -144 ppm remains unaffected. Furthermore, the ^{19}F spin echo spectrum presented in Figure S3 in the Supporting Information reveals that this signal is sharp, suggesting that the F nuclei are in diamagnetic local environments, but with an extended sideband pattern, which presumably results from long-range hyperfine dipolar interactions with the remaining Ni^{3+} ions at 4.6 V. The -144 ppm resonant frequency is in the range of shifts of C=CF groups (typically between -100 and -150 ppm) and of $–CH_2F$ groups (e.g. CF_2H_2 resonates at -143 ppm), which lead us to investigate the possibility of forming surface F as a result of fluorination of the EC and DMC electrolyte solvents at high voltage. Monofluorination of EC leads to fluoroethylene carbonate (FEC) with a reported ^{19}F shift of -123 to -125 ppm[50,51] not observed in any of the spectra collected on the charged samples. Takehara et al.[52] found that the largest product of direct fluorination of DMC is monofluorinated

DMC (MFDMC, 90 % product) with a CH_2F group but with a ^{19}F shift at -158 ppm, also absent from our spectra. A broad ^{19}F NMR signal at -145 ppm was reported by Dupré et al.[51] in an aging study of Si-based anodes. The authors suggested that the -145 ppm signal appearing after one day of exposure of the Si electrodes to the electrolyte (1 M $LiPF_6$ in EC and diethyl carbonate (DEC) with 10 wt% of FEC additive) at 55°C might correspond to a lithiated decomposition product of the FEC additive. This scenario is unlikely in the present work. First because electrolyte decomposition mechanisms taking place upon contact with positive and negative electrodes, and on electrochemical cycling vs. aging, are very different. Second because there is no evidence for the formation of FEC in our cycled samples and our -144 ppm signal is a lot sharper than the broad signal reported previously. We also note that differential electrochemical mass spectrometry (DEMS) measurements on the LNF15 electrode did not detect the formation of F_2 gas on cycling[4] and no F_2 gas signal was observed at -154 ppm[49] in the ^{19}F NMR data. These results suggest that electrolyte degradation pathways inducing F_2/HF gas formation (e.g. as in the hydrolysis of $LiPF_6$[49]) are minor in the electrochemical cell. Overall, there is no evidence supporting the assignment of the -144 ppm peak to surface F species, and the fact that the -144 ppm signal is stable in air but disappears at low potentials suggests that it may correspond to a bulk F environment. Hence, we proceed to investigate the reversible formation of diamagnetic F environments in the bulk of the LNF15 material on charge.

Both Ni L-edge soft X-ray absorption spectroscopy data on LNF15 presented in a previous study by Lee et al.[4] and the MC simulation results on $Li_{1.166-x}Ni_{0.333}Ti_{0.5}O_{1.833}F_{0.166}$ shown in Figure 4b indicate that although the Ni redox reservoir is only partially used on charge, some Ni^{4+} is formed on Li deintercalation. Since Ni^{4+} is diamagnetic, we must expect an increase in the number of diamagnetic F environments surrounded by Li^+, Ti^{4+}, Mo^{6+} and Ni^{4+} ions in the first few metal coordination shells. In addition, NMR signals arising from the significant number of F nuclei directly bonded to one Ni, too broad to be observed in the spectrum of the as-synthesized cathode, are expected to appear upon oxidation of the nearest-neighbor Ni to Ni^{4+}. Since the -144 ppm ^{19}F signal appears at 4.4 V on charge (see Figure 6), i.e. in the voltage range where most Ni ions directly bonded to F are expected to be oxidized (see Figure 4b) and where F species are mostly four-coordinate octahedral and tetrahedral (Figure 5), we tentatively assign it

to four-coordinate F in essentially diamagnetic local environments with or without Ni in the first metal coordination shell. The lower coordination number of these sites, as compared to diamagnetic F in octahedral LiF-like environments, could potentially explain the differences in resonant frequencies (-144 ppm vs. -204 ppm).

Overall, our theoretical results suggest that F impacts the electrochemical properties of LNF15 at the local level by changing the propensity for Ni ions directly bonded to F to form Ni^{3+} before oxidizing to Ni^{4+}, as compared with direct Ni^{2+} -> Ni^{4+} oxidation in oxide-like Ni-O_6 environments. Our MC simulations reveal the formation of four- and five-coordinate F on Li extraction, which is consistent with F incorporation into Li-rich environments in the pristine compound. The appearance of new ^{19}F NMR peaks at high voltage, which do not match any F signal reported for typical SEI phases, may tentatively be ascribed to the formation of undercoordinated octahedral and/or tetrahedral F in diamagnetic environments on Li extraction and Ni oxidation to Ni^{4+}.

Discussion - Consequence of fluorination on the electrochemistry at the local level

A study on F substitution for O in a series of Li-excess cation-disordered Li-Mn-V-O-F cathodes[53] demonstrated that, as F incorporated in Li-rich environments in the as-synthesized material becomes highly undercoordinated on delithiation, it binds more strongly to the remaining Li^+ ions around it and increases their extraction potential. Here, we find that F doping also affects the redox mechanism and potential of the transition metal. Indeed, as shown in Figure 4b, Ni ions directly bonded to at least one F tend to be oxidized stepwise as Ni^{2+} -> Ni^{3+} -> Ni^{4+}, rather than directly oxidizing from Ni^{2+} to Ni^{4+} through Ni^{3+} disproportionation. This result is consistent from a molecular orbital diagram prospective, as an increase in electronegativity of the ligand atom ($\chi_F > \chi_O$) pushes the ligand orbitals lower in energy, resulting in less efficient overlap between the metal (M) and ligand (L) orbitals and a more ionic M-L bond with a smaller energy difference between the t_{2g} and e_g^* orbitals. In turn, this leads to a lower energy e_g^* frontier orbital

and a higher oxidation potential required to extract electrons to form Ni^{4+} versus Ni^{3+}. The effect may also be geometric as Ni^{3+} is a Jahn-Teller active ion and thus requires distortion of its local environment. As Ni^{2+} and Ni^{4+} are not Jahn-Teller active and do not support this type of distortion, Ni^{3+} formation in pure oxides may be suppressed by the energy required to impose strain on its environment. Fluorination perturbs the symmetry of the Ni^{2+} octahedra and may thus facilitate the formation of Ni^{3+}. Note however that the change in Ni oxidation behavior we observe in our computational model is not due to any Ni migration and associated changes in the Ni crystal field during delithiation. Supplementary Figure S5 shows the distribution of Ni coordination number across the voltage curve, illustrating that Ni predominantly retains its 6-fold octahedral coordination throughout delithiation, up to some local distortion. While we do observe rare formation of tetrahedral Ni in pure oxide environments, the population of these Ni centers is far too low to account for our observations.

The promotion of Ni^{3+} formation upon fluorination is expected to increase the utilization of the $Ni^{2+/4+}$ redox reservoir. Given that our calculations show that no more than 60% of the Ni may be oxidized to Ni^{4+} due to overlap between the O and Ni valence states, promoting Ni^{3+} formation from Ni^{2+} increases the maximum attainable Ni capacity from 60% of the $Ni^{2+/4+}$ reservoir for Ni-O_6 sites (40% Ni^{2+}, 60% Ni^{4+} at the top of charge) to 80% (40% Ni^{3+}, 60% Ni^{4+} at the top of charge) for Ni-O_5F sites. Unfortunately, a direct comparison of the electrochemical properties of LN15 vs. LNF15 presented previously[4] does not enable us to confirm this effect experimentally, because of the greater Ni content in LNF15, also increasing the useable Ni redox capacity, and the difficulty to distinguish between Ni^{3+} vs. Ni^{4+} formation unambiguously using XAS on disordered materials.

To summarize, on the one hand, F doping leads to more redox-active Ni^{2+} in the pristine LNF15 cathode, which in turn increases the Ni-based redox capacity and reduces both the amount O that participates in the charge compensation mechanisms and the amount of O loss on charge.[4] In the present paper, we show that F^- anions directly bonded to Ni (F in F-Ni environments) change the Ni redox mechanism from $Ni^{2+} \rightarrow Ni^{4+}$ to $Ni^{2+} \rightarrow Ni^{3+} \rightarrow Ni^{4+}$, effectively increasing the useable Ni redox capacity. In addition, by lowering the average anion charge in the compound, F doping is an efficient way of introducing

low-valent Li excess in the material without the need for high-valent metal charge compensators.[53] On the other hand, the presence of undercoordinated F at high voltage (F in FLi_6 environments) leads to Li gettering, as was recently studied in great detail by Kitchaev et al.[53] This study showed that 0.4-0.8 Li per F in Li-Mn-V-O-F rocksalt cathodes is inaccessible at moderate voltages because of strong Li-F binding. We expect that a similar fraction of Li will be inaccessible in our LNF15 cathode. This work and previous studies clearly indicate that F substitution for O has both benefits and drawbacks in terms of electrochemical performance, and the design of high-performance oxyfluoride rocksalt cathodes requires careful optimization of the amount of F, Li and redox-active metal species in the material. The present study also demonstrates that F-Ni and FLi_6 F environments have very different effects on the properties of the LNF15 cathode, suggesting that the relative proportion of the different F local environments in the cathode is yet another important aspect to consider.

Conclusion

In this work, we demonstrated that a combination of Monte Carlo simulations, density functional theory (DFT) calculations and solid-state Nuclear Magnetic Resonance (NMR) can provide tremendous insight into the impact of fluorination on the short-range order in the Li-excess cation-disordered $Li_{1.15}Ni_{0.45}Ti_{0.3}Mo_{0.1}O_{1.85}F_{0.15}$ (LNF15) cathode, and into the changes in the local F environments and the redox mechanisms taking place on electrochemical cycling. Our Monte Carlo simulations on the $Li_{1.166}Ni_{0.333}Ti_{0.5}O_{1.833}F_{0.166}$ model structure suggest that F substitution introduces short-range order and F is incorporated in Li-rich sites with five or six Li nearest-neighbors. While strong paramagnetic broadening of the ^{19}F NMR signal prevents the detection of F directly bonded to $Ni^{2+/3+}$, F environments with no $Ni^{2+/3+}$ nearest-neighbors are clearly observed in the ^{19}F NMR spectra. The electrochemical curve computed with DFT on a series of $Li_{1.166-x}Ni_{0.333}Ti_{0.5}O_{1.833}F_{0.166}$ stable structures determined from Monte Carlo simulations at different levels of delithiation is in excellent agreement with the experimental charge curve obtained for shaker-milled S-LNF15 cathode, confirming that our simulations successfully encapsulate the structural

and electronic phenomena taking place in the real material. Close inspection of the $Li_{1.166-x}Ni_{0.333}Ti_{0.5}O_{1.833}F_{0.166}$ stable structures reveals that Li extraction leads to four- and five-coordinate F environments. We speculate that Ni oxidation to Ni^{4+}, leading to a greater number of diamagnetic F sites on charge, and the formation of undercoordinated octahedral and/or tetrahedral F environments, could account for the appearance of new ^{19}F NMR signals at 4.4 and 4.6 V charge for LNF15. Our calculations further indicate that partial Ni oxidation takes place on charge, accompanied by O oxidation from 4.4-4.5 V. Interestingly, our theoretical results show that Ni ions with Ni-F bonds follow a different oxidation mechanism than those in NiO_6 octahedra, forming Ni^{3+} intermediates instead of oxidizing from Ni^{2+} to Ni^{4+}. While the oxidation of Ni^{2+} towards Ni^{4+} is incomplete in oxides, due to overlap between the O and Ni valence states, these results suggest that fluorination may be an efficient strategy to utilize the Ni^{2+}/Ni^{4+} redox reservoir to a greater extent. In turn, a better use of the transition metal redox reservoir is expected to reduce the amount of O oxidation and potential O loss at the end of charge, leading to more reversible electronic and structural processes during electrochemical cycling.

Supporting Information

Additional details on hybrid DFT/HF calculations of paramagnetic NMR parameters. Magnetic susceptibility measurements on LNF15 and LN15. Determination of the magnetic scaling factor Φ. Additional solid-state NMR data: ^{7}Li pj-MATPASS isotropic spectra obtained at different stages of charge on LNF15 and LN15 electrode films; ^{19}F pj-MATPASS isotropic spectra obtained on the 4.6 V charged LNF15 sample before and after air exposure; ^{19}F spin echo spectrum acquired on the 4.6 V charge LNF15 sample.

Acknowledgements

This work was supported by the Assistant Secretary for Energy Efficiency and Renewable Energy, Vehicle Technologies Office, of the U.S. Department of Energy under Contract No. DE-AC02-05CH11231, under the Advanced Battery Materials Research (BMR) Program. Work by R.J.C, D.A.K. and J.L. was also supported by Robert Bosch LLC and Umicore Specialty Oxides and Chemicals. The authors thank Zhengyan Lun his help with sample preparation. R.J.C. would also like to acknowledge Dr. Leo Lamontagne for his help with the magnetic susceptibility measurements and Dr. Jerry Hu for his assistance in setting up the NMR experiments. The authors would like to acknowledge the California NanoSystems Institute (CNSI) at the University of California Santa Barbara (UCSB) for experimental time on the 500

MHz NMR spectrometer. The NMR experimental work reported here made use of the shared facilities of the UCSB MRSEC (NSF DMR 1720256), a member of the Material Research Facilities Network. Computational resources were provided by Department of Energy's Office of Energy Efficiency and Renewable Energy and located at the National Renewable Energy Laboratory, as well as the National Energy Research Scientific Computing Center, a DOE Office of Science User Facility supported by the Office of Science of the U.S. Department of Energy under Contract No. DE-AC02-05CH11231.

References

(1) Lee, J.; Urban, A.; Li, X.; Su, D.; Hautier, G.; Ceder, G. *Science* **2014**, *343* (6170), 519.

(2) Urban, A.; Lee, J.; Ceder, G. *Adv. Energy Mater.* **2014**, *4* (13), 1400478.

(3) Croguennec, L.; Palacin, M. R. *J. Am. Chem. Soc.* **2015**, *137* (9), 3140.

(4) Lee, J.; Papp, J. K.; Clément, R. J.; Sallis, S.; Kwon, D.-H.; Shi, T.; Yang, W.; McCloskey, B. D.; Ceder, G. *Nat. Commun.* **2017**, *8* (1), 190.

(5) Genevois, C.; Koga, H.; Croguennec, L.; Ménétrier, M.; Delmas, C.; Weill, F. *J. Phys. Chem. C* **2015**, *119* (1), 75.

(6) Yan, P.; Nie, A.; Zheng, J.; Zhou, Y.; Lu, D.; Zhang, X.; Xu, R.; Belharouak, I.; Zu, X.; Xiao, J.; Amine, K.; Liu, J.; Gao, F.; Shahbazian-Yassar, R.; Zhang, J.-G.; Wang, C.-M. *Nano Lett.* **2015**, *15* (1), 514.

(7) Qian, D.; Xu, B.; Chi, M.; Meng, Y. S. *Phys. Chem. Chem. Phys.* **2014**, *16* (28), 14665.

(8) Lee, J.; Seo, D.-H.; Balasubramanian, M.; Twu, N.; Li, X.; Ceder, G. *Energy Environ. Sci.* **2015**, *8* (11), 3255.

(9) Grey, C. P.; Dupré, N. *Chem. Rev.* **2004**, *104* (10), 4493.

(10) Carlier, D.; Ménétrier, M.; Grey, C.; Delmas, C.; Ceder, G. *Phys. Rev. B* **2003**, *67* (17), 174103.

(11) Kim, J.; Middlemiss, D. S.; Chernova, N. A.; Zhu, B. Y. X.; Masquelier, C.; Grey, C. P. *J. Am. Chem. Soc.* **2010**, *132* (47), 16825.

(12) Middlemiss, D. S.; Ilott, A. J.; Clément, R. J.; Strobridge, F. C.; Grey, C. P. *Chem. Mater.* **2013**, *25* (9), 1723.

(13) Clément, R. J.; Pell, A. J.; Middlemiss, D. S.; Strobridge, F. C.; Miller, J. K.; Whittingham, M. S.; Emsley, L.; Grey, C. P.; Pintacuda, G. *J. Am. Chem. Soc.* **2012**, *134* (41), 17178.

(14) Pan, C.; Lee, Y. J.; Ammundsen, B.; Grey, C. P. *Chem. Mater.* **2002**, *14* (5), 2289.

(15) Yoon, W.-S.; Iannopollo, S.; Grey, C. P.; Carlier, D.; Gorman, J.; Reed, J.; Ceder, G. *Electrochem. Solid-State Lett.* **2004**, *7* (7), A167.

(16) Jiang, M.; Key, B.; Meng, Y. S.; Grey, C. P. *Chem. Mater.* **2009**, *21* (13), 2733.

(17) Xu, J.; Lee, D. H.; Clément, R. J.; Yu, X.; Leskes, M.; Pell, A. J.; Pintacuda, G.; Yang, X.-Q.; Grey, C. P.; Meng, Y. S. *Chem. Mater.* **2014**, *26* (2), 1260.

(18) Clément, R. J.; Middlemiss, D. S.; Seymour, I. D.; Ilott, A. J.; Grey, C. P. *Chem. Mater.* **2016**, *28* (22), 8228.

(19) Clément, R. J.; Xu, J.; Middlemiss, D. S.; Alvarado, J.; Ma, C.; Meng, Y. S.; Grey, C. P. *J. Mater. Chem. A* **2017**, *5* (8), 4129.

(20) Chen, R.; Ren, S.; Knapp, M.; Wang, D.; Witter, R.; Fichtner, M.; Hahn, H. *Adv. Energy Mater.* **2015**, *5* (9), 1401814.

(21) Harris, K. J.; Foster, J. M.; Tessaro, M. Z.; Jiang, M.; Yang, X.; Wu, Y.; Protas, B.; Goward, G. R. *Chem. Mater.* **2017**, *29* (13), 5550.

(22) Fontaine, D. D. *Solid State Physics* **1994**, *47*, 33.

(23) Richards, W. D.; Wang, Y.; Miara, L. J.; Kim, J. C.; Ceder, G. *Energy Environ. Sci.* **2016**, *9* (10), 3272.

(24) Nelson, L. J.; Hart, G. L. W.; Fei, Z.; Ozoliņš, V. *Phys. Rev. B* **2013**, *87* (3), 035125.

(25) Kresse, G.; Joubert, D. *Phys. Rev. B* **1999**, *59* (3), 1758.

(26) Kresse, G.; Furthmüller, J. *Comput. Mater. Sci.* **1996**, *6* (1), 15.

(27) Perdew, J. P.; Burke, K.; Ernzerhof, M. *Phys. Rev. Lett.* **1996**, *77* (18), 3865.

(28) Wang, L.; Maxisch, T.; Ceder, G. *Phys. Rev. B* **2006**, *73* (19), 195107.

(29) Sun, J.; Ruzsinszky, A.; Perdew, J. P. *Phys. Rev. Lett.* **2015**, *115* (3), 036402.

(30) Kitchaev, D. A.; Peng, H.; Liu, Y.; Sun, J.; Perdew, J. P.; Ceder, G. *Phys. Rev. B* **2016**, *93* (4), 045132.

(31) Zhang, Y.; Kitchaev, D. A.; Yang, J.; Chen, T.; Dacek, S. T.; Sarmiento-Pérez, R. A.; Marques, M. A. L.; Peng, H.; Ceder, G.; Perdew, J. P.; Sun, J. *npj Computational Materials* **2018**, *4* (1), 9.

(32) Heyd, J.; Scuseria, G. E.; Ernzerhof, M. *J. Chem. Phys.* **2003**, *118* (18), 8207.

(33) Seo, D.-H.; Urban, A.; Ceder, G. *Phys. Rev. B* **2015**, *92* (11), 115118.

(34) Ong, S. P.; Richards, W. D.; Jain, A.; Hautier, G.; Kocher, M.; Cholia, S.; Gunter, D.; Chevrier, V. L.; Persson, K. A.; Ceder, G. *Comput. Mater. Sci.* **2013**, *68* (C), 314.

(35) Hung, I.; Zhou, L.; Pourpoint, F.; Grey, C. P.; Gan, Z. *J. Am. Chem. Soc.* **2012**, *134* (4), 1898.

(36) Strobridge, F. C.; Middlemiss, D. S.; Pell, A. J.; Leskes, M.; Clément, R. J.; Pourpoint, F.; Lu, Z.; Hanna, J. V.; Pintacuda, G.; Emsley, L.; Samoson, A.; Grey, C. P. *J. Mater. Chem. A* **2014**, *2* (30), 11948.

(37) Strobridge, F. C.; Clément, R. J.; Leskes, M.; Middlemiss, D. S.; Borkiewicz, O. J.; Wiaderek, K. M.; Chapman, K. W.; Chupas, P. J.; Grey, C. P. *Chem. Mater.* **2014**, *26* (21), 6193.

(38) Dovesi, R.; Orlando, R.; Erba, A.; Zicovich-Wilson, C. M.; Civalleri, B.; Casassa, S.; Maschio, L.; Ferrabone, M.; La Pierre, De, M.; D'Arco, P.; Noël, Y.; Causà, M.; Rérat, M.; Kirtman, B. *Int. J. Quantum Chem.* **2014**, *114* (19), 1287.

(39) Ménétrier, M.; Bains, J.; Croguennec, L.; Flambard, A.; Bekaert, E.; Jordy, C.; Biensan, P.; Delmas, C. *J. Solid State Chem.* **2008**, *181* (12), 3303.

(40) Croguennec, L.; Bains, J.; Ménétrier, M.; Flambard, A.; Bekaert, E.; Jordy, C.; Biensan, P.; Delmas, C. *J. Electrochem. Soc.* **2009**, *156* (5), A349.

(41) Richards, W. D.; Dacek, S. T.; Kitchaev, D. A.; Ceder, G. *Adv. Energy Mater.* **2017**, 1701533.

(42) Seymour, I. D.; Middlemiss, D. S.; Halat, D. M.; Trease, N. M.; Pell, A. J.; Grey, C. P. *J. Am. Chem. Soc.* **2016**, *138* (30), 9405.

(43) Yabuuchi, N.; Takeuchi, M.; Nakayama, M.; Shiiba, H.; Ogawa, M.; Nakayama, K.; Ohta, T.; Endo, D.; Ozaki, T.; Inamasu, T.; Sato, K.; Komaba, S. *Proc. Natl. Acad. Sci. U.S.A.* **2015**, *112* (25), 7650.

(44) Hoshino, S.; Glushenkov, A. M.; Ichikawa, S.; Ozaki, T.; Inamasu, T.; Yabuuchi, N. *ACS Energy Letters* **2017**, *2* (4), 733.

(45) Chung, J. H.; Lim, J. H.; Shin, Y. J.; Kang, J. S.; Jaiswal-Nagar, D.; Kim, K. H. *Phys. Rev. B* **2008**, *78* (21), 783.

(46) Wawrzyńska, E.; Coldea, R.; Wheeler, E. M.; Sörgel, T.; Jansen, M.; Ibberson, R. M.; Radaelli, P. G.; Koza, M. M. *Phys. Rev. B* **2008**, *77* (9), 701.

(47) Chen, H.; Freeman, C. L.; Harding, J. H. *Phys. Rev. B* **2011**, *84* (8), 085108.

(48) Michan, A. L.; Divitini, G.; Pell, A. J.; Leskes, M.; Ducati, C.; Grey, C. P. *J. Am. Chem. Soc.* **2016**, *138* (25), 7918.

(49) Plakhotnyk, A. V.; Ernst, L.; Schmutzler, R. *J. Fluorine Chem.* **2005**, *126* (1), 27.

(50) Markevich, E.; Fridman, K.; Sharabi, R.; Elazari, R.; Salitra, G.; Gottlieb, H. E.; Gershinsky, G.; Garsuch, A.; Semrau, G.; Schmidt, M. A.; Aurbach, D. *J. Electrochem. Soc.* **2013**, *160* (10), A1824.

(51) Dupre, N.; Moreau, P.; De Vito, E.; Quazuguel, L.; Boniface, M.; Bordes, A.; Rudisch, C.; Bayle-Guillemaud, P.; Guyomard, D. *Chem. Mater.* **2016**, *28* (8), 2557.

(52) Takehara, M.; Watanabe, S.; Nanbu, N.; Ue, M.; Sasaki, Y. *Synth. Commun.* **2004**, *34* (8), 1367.

(53) Kitchaev, D. A.; Lun, Z.; Richards, W.; Ji, H.; Clément, R. J.; Balasubramanian, M.; Kwon, D.-H.; Dai, K.; Papp, J. K.; Lei, T.; McCloskey, B. D.; Yang, W.; Lee, J.; Ceder, G. *Energy Environ. Sci.* **2018**, accepted manuscript, DOI: 10.1039/C8EE00902C.

For Table of Contents Only: